Journal of Hydrology 608 (2022) 127681

Contents lists available at ScienceDirect

Journal of Hydrology

journal homepage: www.elsevier.com/locate/jhydrol

Research papers

Image-based machine learning for monitoring the dynamics of the largest salt marsh in the Yangtze River Delta

Yaying Lou [a], Zhijun Dai [a,b,*], Chuqi Long [a], Hui Dong [c], Wen Wei [a], Zhenming Ge [a]

[a] State Key Laboratory of Estuarine and Coastal Research, East China Normal University, Shanghai 200062, China
[b] Laboratory for Marine Geology, Qingdao National Laboratory for Marine Science and Technology, Qingdao 266061, China
[c] Eastern Navigation Service Center, Maritime Safety Administration, the People's Republic of China, Shanghai 200090, China

ARTICLE INFO

This manuscript was handled by Marco Borga, Editor-in-Chief, with the assistance of Marco Toffolon, Associate Editor

Keywords:
Salt marsh
Mudflat
Morphodynamics
Sea-level rising
Changjiang (Yangtze) Delta

ABSTRACT

The extreme decline in fluvial sediment discharge and rapid increase in sea level have increased salt marsh vulnerability in some of the world's mega-delta. However, limited research has addressed both the vertical accretion and horizontal/lateral progradation of salt marshes induced by anthropogenic activities in recent decades. Here, a machine learning-based method for retrieving remote sensing images of the salt marsh along the Eastern Chongming Wetland (ECW), the largest wetland in the Yangtze River Delta, was used to monitor salt marsh dynamics between 2002 and 2019. The results demonstrate that salt marshes have experienced significant expansion, including seaward progradation and accretion with ranges of −18.5–60.6 m/yr and 0.103–0.178 m/yr, respectively. Nevertheless, the bare mudflat areas adjoining the salt marshes have remained almost unchanged, while their progradation and accretion have also shown similar trends with the ranges of −13.3–103.7 m/yr, and 0.066–0.256 m/yr, respectively. Although there was a 70% reduction in fluvial sediment supply in the Yangtze River Delta after the Three Gorges Dam (TGD) began operating in 2003, it is less understood if the constant local suspended sediment concentration (SSC) of the estuary could be responsible for supporting enough sediment to enable salt marsh and mudflat expansions. Meanwhile, the results showed that the seaward expansion of the mudflats provided suitable space for the salt marsh to trap vast amounts of sediment and gradually occupy the adjoining mudflat area. The mudflat progradation further provided a larger space for the growth of salt marsh vegetation and promoted salt marsh expansion. Moreover, the accretion of the ECW indicates the high resilience of these salt marshes to sea-level rise (SLR). The present work highlights the external factors and internal driving forces of the salt marsh evolution process, providing information that can be used by communities and coastal managers to conserve and restore the salt marshes in the future.

1. Introduction

Estuarine salt marshes, located in the intertidal zone of transition, are among the most valuable coastal geomorphic features (Barbier et al., 2008, 2011; Vuik et al., 2016). As economically significant natural resources on Earth, they provide habitats for fish and wildlife species and land resources for social and economic development and provide coastal stability against flood risks from land and ocean (Allen, 2000; Costanza, 2006; Murray et al., 2012). Therefore, salt marsh dynamics have caused widespread concern worldwide (Huang et al., 2010; Spencer et al., 2016; Murray et al., 2019).

However, some studies have indicated that land subsidence, sea-level rise (SLR), coastal development, and decreased fluvial suspended sediment discharge (SSD) have induced large-scale salt marsh degradation (Spencer et al., 2016; Wei et al., 2017; Murray et al., 2019), such as in the Mississippi Estuary (Reed, 2002), Chesapeake Bay (Kearney et al., 2002), Venice Lagoon (Carniello et al. 2009), and the Yellow Sea Estuary (Murray et al., 2014). Specifically, Spencer et al. (2016) predicted that 78% of global coastal wetlands would be lost given the coupling influence between accelerated SLR (110 cm by 2100) and dike construction, and this estimate was based on the Dynamic Interactive Vulnerability Assessment Wetland Change Model. In Louisiana, Jankowski et al. (2017) determined that 35% of the wetlands in the Mississippi Delta (SE Louisiana) and 58% of the sites on the Chenier Plain (SW Louisiana) may experience erosion and degradation risks at a relative SLR rate of 12 ± 8 mm per year. Subsequently, Gu et al. (2018)

* Corresponding author at: State Key Laboratory of Estuarine and Coastal Research, East China Normal University, Shanghai 200062, China.
E-mail address: zjdai@sklec.ecnu.edu.cn (Z. Dai).

https://doi.org/10.1016/j.jhydrol.2022.127681
Received 5 August 2021; Received in revised form 17 February 2022; Accepted 27 February 2022
Available online 3 March 2022

also indicated that with the impact of the SLR and coastal reclamation, severe losses (59%) of salt marshes occurred in China from the 1980 s to the 2010 s. In contrast, Kirwan et al. (2016) stated that salt marsh vulnerability was overstated and that marsh accretion could exceed the relative SLR (10 mm/yr), as higher tidal inundation promotes more settling of sediments and hence accretion, where plants further contribute by trapping sediments and adding organic matter accretion. In the Plum Island Estuary (Massachusetts, USA), Langston et al. (2020) demonstrated that salt marshes were not immediately vulnerable to erosion despite their inadequate sediment supply and SLR, as sediment accumulation contributes to salt marsh elevation (Langston et al., 2020). Furthermore, based on the integrated global modeling approach, a recent study showed that the global extent of marshes would increase to 60% of the current area until 2100 if the wetlands have sufficient coastal accommodation space and the present level of sediment supply remains the same (Schuerch et al. 2018). These different research results highlight that whether coastal wetland degradation or progradation occurs with the relative SLR or reduction of fluvial sediment is still undetermined. Moreover, a few studies have proposed that the local sediment fluxes toward salt marshes are crucial for marsh survival (Ladd et al., 2019; Fagherazzi et al., 2020). However, salt marsh dynamics that consist of accretion and progradation changes are determined by multiple complex effects related to global changes, and there is a need to gain greater insight into the marsh's morphodynamic processes.

The determination of salt marsh morphodynamics in previous studies has mainly been analyzed by field observations (Tang et al., 2015), digital elevation model construction (Shaw et al., 2016), and the creation of hydrodynamic-morphodynamic models (Nardin et al., 2016). Nevertheless, the above mentioned traditional methods for observing mudflats and salt marshes are time-consuming and involve labor-intensive measurements. Based on these limitations, it is difficult to carry out large-scale and long-term salt marsh landform detection (Murray et al., 2012). More specifically, to determine salt marsh dynamics in terms of SLR influence, decades of data records are required, which is impractical to obtain through tidal flat profile observations. At the same time, it is challenging to link the biological factors, hydrodynamics, and geomorphology of salt marshes through model construction because salt marshes are intimately related to mudflats (Carlin and Dellapenna 2014). Compared with traditional methods that are expensive and have regional limitations, remote sensing technology is recognized as an efficient tool for monitoring salt marsh morphodynamics (Anthony et al., 2015).

The Changjiang Delta (CJD) (Yangtze River Delta) is one of the largest deltas in Asia and has multiple vast estuarine wetlands, where the Eastern Chongming wetland (ECW) contains the largest salt marsh of the CJD (Chen et al., 1985) (Fig. 1). The ECW receives substantial sediment input from the Changjiang River (Wei et al., 2016). In recent decades, the ECW has faced large challenges related to riverine suspended sediment discharge (SSD) reductions and SLR impacts (Tian et al., 2010; Dai et al., 2014). With the construction of the largest dam in the world, the Three Gorges Dam (TGD), finalized in 2003, fluvial sediment input has remarkably decreased by over 70% (Dai et al., 2014). Furthermore, the coupling effects between the sharp reduction in riverine SSD and relative SLR could further induce potential erosion risks for the ECW salt marshes (Yang et al., 2020; Leonardi et al., 2021; Dai, 2021). Tian et al. (2010) indicated that under the IPCC sea-level rise scenarios (0.88 m increase in 2100), 40% of the Chongming wetland area would be inundated, especially the *Scirpus mariqueter* communities and mudflats. Li et al. (2014) noted that the salt marshes of the CJD had slower seaward migration rates after 2003 due to the decline in the fluvial SSD. In addition, utilizing field measurements, Yang et al. (2020) found that the salt marshes in the CJD exhibited an accretion trend, which could balance the relative SLR. Recent work also indicated that the ECW could survive for years to decades under declining riverine SSD conditions due to the support of abundant sediment from the submarine delta (Yang et al., 2021).

However, the previous work that referred to the salt marshes in the ECW could have one-sided views and not reflect the recognition of all the ECW's salt marsh dynamics, even though they mentioned potential impacts to salt marshes from riverine SSD decline and SLR. Specifically,

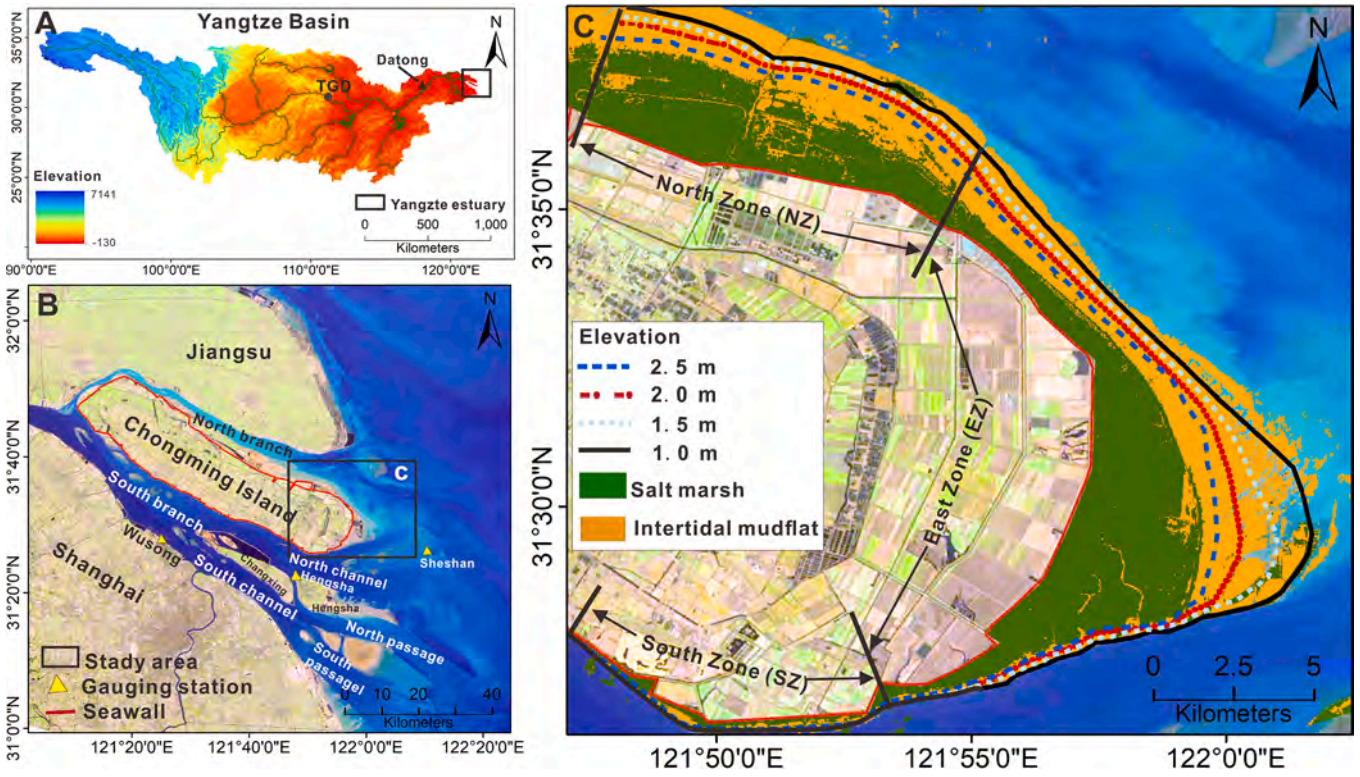

Fig. 1. Study area of the Eastern Chongming wetland and distribution of the salt marsh areas and mudflat areas.

the work analyzing monthly elevation data over 8 years (2005–2013) based on three fixed stations in one profile at the center of the ECW was too short; thus, it was limited in its representation of the whole ECW salt marsh response to SLR (Yang et al., 2020). Additionally, two isobaths of −2 m and −5 m collected in 1997, 2002, and 2010 as documented in Yang et al. (2021) may also not adequately reflect the variations in the salt marshes because of the suitable growth elevations of salt marshes above 2 m (Ge et al., 2015a; Ge et al., 2015b). To date, there is a great obstacle to obtaining long-term elevation data in salt marshes, which are key to exploring the relationship between salt marsh variations and SLR (Murray et al., 2012). The erosion or accretion of salt marshes in response to SLR and insufficient sediment not only is recognized as a long-term process due to sediment settling lag/scour lag effects but also depends on local hydrogeomorphological conditions (Anthony and Dobroniak, 2000; Fagherazzi et al., 2020). Therefore, it is essential to have a comprehensive understanding of the ECW's response to external forcings based on long-term systematic data.

Little information is available on how the abovementioned forcings impact ECW salt marsh dynamics and the potential couplings between salt marshes and mudflats in this region. In this study, we try to fill gaps in monitoring the successive dynamics of the salt marsh-mudflat system in the ECW to determine the vegetation-geomorphology interaction process based on long-term data by an effective method. Therefore, new machine learning approaches that interpret large numbers of remote sensing images and then combine them with the 17-year hourly tidal elevations to construct a conceptual tidal flat model were used in this work. Utilizing this comprehensive methodology with data collection on decadal salt marsh dynamics, the main aim was to (1) detect the long-term dynamics of the salt marshes of the ECW; (2) determine the main driving forces of salt marsh dynamics; and (3) discriminate couplings between salt marsh dynamics and variations in the mudflats. This work provides a vital foundation for managing risk in global mega-deltas, as they respond to similar environmental effects.

2. Materials and methods

2.1. Study area

The Changjiang Estuary (CJE) is an irregular semidiurnal tidal estuary, and its average daily tidal range is 2.67 m (Dai et al., 2013a). The subtropical monsoon climate of this region results in significant seasonal wind direction variations, with wind directions of NW-NNW in winter and of SSE-S in summer and average wind speeds of 4.5–7.2 m/s (Yun, 2004). The wind in the CJE is the dominant factor affecting wave activities, including wave directions and heights. Yun (2004) proposed that the average wave height at the Sheshan station could reach 0.9 m based on long-term observation records.

The ECW is one of the most extensive wetlands in the CJE, located in the slow-flowing zone between the North Branch and the North Channel of this estuary (Dai et al., 2018a) (Fig. 1). The suspended sediment concentration (SSC) of the surrounding area is approximately 0.42 kg/m^3 (Chen et al., 2004). As a result of Chongming Island shadow effects, the ECW is well developed and has continued to expand seaward for the past decades (Wei et al., 2017), with a width of more than 7 km at the tip, featuring a vegetated salt marsh and mudflat. Fine sand (median diameter of 8–15 μm) and mud are the major components of the surficial sediments in this area (Yan et al., 2011). There are three primary vegetation communities in this salt marsh zone: *Phragmites australis*, *Scirpus mariqueter*, and *Spartina alterniflora* (Ge et al., 2015a; Ge et al., 2015b). *Phragmites australis* and *Scirpus mariqueter* are native species, while *Spartina alterniflora* was introduced in the eastern Chongming flat in 1995 and has rapidly spread due to its extraordinary competitive ability (Yuan et al., 2011).

In addition, considering the distinct regional features in the ECW, this work divided the whole wetland into three zones to describe the local wetland dynamics in detail (Fig. 1). Specifically, the South Zone (SZ) of the ECW has steeper slopes and small salt marshes and mudflats. The East Zone (EZ), with a gentle slope, has a large area of salt marshes and mudflats, whereas the regional features of the North Zone (NZ) are between those of the SZ and EZ.

2.2. Data collection

According to the Worldwide Reference System, one Landsat image (path 118, Row 38) completely covers Chongming Island (Fig. 1). A total of 161 Landsat images with cloud cover < 50% from 2002 to 2019 were obtained from the Google Earth Engine (GEE), including Landsat − 5 TM (2002–2011), − 7 ETM (2002–2003), and − 8 OLI images (2013–2019) (Table 1). These data are identified as the standard Level 1 terrain-corrected (L1T) products that have been revised through the Landsat ecosystem disturbance adaptive processing system (LEADAPS) and Landsat surface reflectance code (LaSRC) (Vermote et al., 2016). All of these L1T products are recognized as being high quality and ready-to-use (Chen et al., 2017).

The hourly tidal level data from 2002 to 2019 at Hengsha station (using the theoretical minimum tidal surface as the benchmark) were acquired from the China Oceanic Information Network (https://www.coi.gov.cn/) and applied to map the tidal mudflats under different tidal levels. The annual runoff and SSD at Datong station (the most downstream hydrologic station in the Changjiang River) were obtained from the Changjiang Water Resource Committee (http://www.cjw.gov.cn/zwzc/bmgb/nsgb). The wave direction data from 1979 to 2018 were downloaded from the European Centre for Medium-Range Weather Forecasts (ECMWF) (https://apps.ecmwf.int/datasets/data/interim-full-daily/levtype=sfc/). These hydrological data are considered the main driving factors of tidal mudflat evolution.

2.3. Methods

2.3.1. Reference sample selection

To explore the evolution of the salt marshes and mudflats, we categorized the Eastern Chongming wetland as salt marsh, mudflat, and water. The annual Landsat images with the lowest cloud cover were selected to generate training samples using visual interpretation. First, we built three layers in GEE and identified them as salt marsh areas, mudflat areas, and water areas. Then, we manually selected dozens of regions of interest (ROIs) in each layer and generated 500 random points by the 'randomPoint' command in GEE. In this study, 3706 ROIs were selected, and 25,500 random sample points were generated, including 1281 salt marsh samples (8500 sample points), 1390 mudflat samples (8500 sample points), and 1035 water area samples (8500 sample points) (Table 2). Seventy percent of these sample points were applied for training, and the remaining points were applied for the accuracy assessment.

2.3.2. Landsat data processing

The pixel-based supervised random forest (RF) algorithm was used to discriminate the different landforms in the Eastern Chongming wetland. Based on the GEE platform, Landsat data processing is divided into three steps: (1) selecting and preprocessing Landsat images, (2) conducting the RF algorithm classification, and (3) identifying different landform area statistics and sketching the edges of the salt marshes and mudflats (Fig. 2).

The Three Gorges Dam (TGD), the largest hydrological project in the

Table 1
Statistical information for the Landsat image collections.

Period	Sensor	Time	Image Count
2002–2011	Landsat 5 TM	2002/1/1–2011/12/31	78
2002–2003	Landsat 7 ETM	2002/1/1–2003/5/31	13
2013–2019	Landsat 8 OLI	2013/4/11–2019/12/31	70

Table 2
Sample numbers of the three land cover types.

Year	Numbers of ROI (salt marsh)	Numbers of ROI (mud flat)	Numbers of ROI (water area)
2002	65	72	42
2003	62	84	45
2004	65	77	56
2005	65	80	70
2006	77	80	70
2007	76	75	68
2008	76	82	65
2009	84	86	68
2010	85	78	64
2011	78	91	65
2013	76	88	63
2014	89	89	63
2015	81	86	63
2016	77	79	57
2017	83	80	58
2018	75	80	61
2019	67	83	57
Total	1281	1390	1035

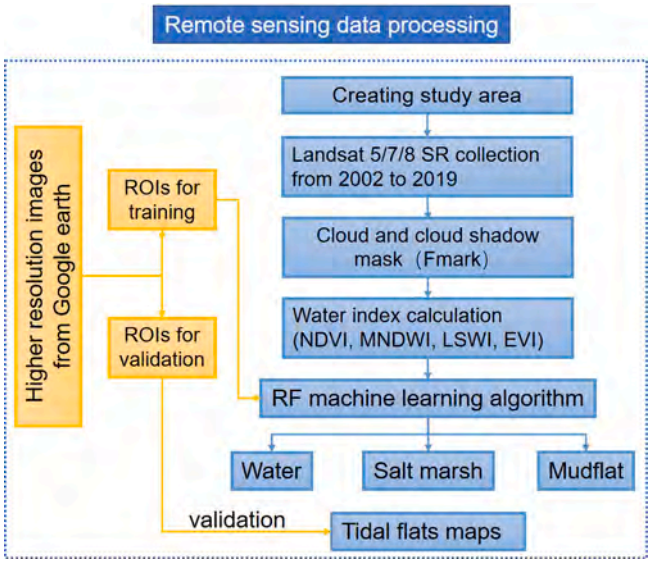

Fig. 2. Workflow of wetland extraction using Landsat images.

world, was constructed in 2003, and caused a sharp decrease in fluvial SSC (Dai et al., 2013b; Dai et al., 2018a). To examine the ECW morphodynamics, all available Landsat images from 2002 to 2019 were collected for this study. The images in 2002 represent the scenario with unchanged fluvial SSC before TGD operation. As clouds and cloud shadows directly affect Landsat image interpretation, we further masked these distractions by using the Fmask algorithm of the GEE and reconstructed more precise observations from the Landsat data (Zhu and Woodcock, 2012; Jia et al., 2021). In addition, various landforms have different spectral characteristics (Huete et al., 2002; Jiang et al., 2015). To effectively classify these spectral characteristics, four water and vegetation indices were applied, such as the normalized difference vegetation index (NDVI) (Tucker, 1979), enhanced vegetation index (EVI) (Huete et al., 2002), land surface water index (LSWI) (Xiao et al., 2004) and modified normalized difference water index (mNDWI) (Xu, 2006).

$$NDVI = \frac{\rho_{NIR} - \rho_{RED}}{\rho_{NIR} + \rho_{RED}} \quad (1)$$

$$EVI = 2.5 \times \frac{\rho_{NIR} - \rho_{RED}}{\rho_{NIR} + 6\rho_{RED} - 7\rho_{BLUE} + 1} \quad (2)$$

$$LSWI = \frac{\rho_{NIR} - \rho_{SWIR}}{\rho_{NIR} + \rho_{SWIR}} \quad (3)$$

$$mNDWI = \frac{\rho_{GREEN} - \rho_{SWIR}}{\rho_{GREEN} + \rho_{SWIR}} \quad (4)$$

where ρ_{BLUE}, ρ_{GREEN}, ρ_{RED}, ρ_{NIR}, ρ_{SWIR} represent the pixel values of the blue (B2), green (B3), red (B4), near-infrared (B5), and shortwave infrared (B6 and B7) bands of the Landsat images, respectively.

Then, 11 bands (seven spectral reflectance bands and four index bands) constituted the input datasets of this RF algorithm to boost the between-class separability of the various land cover types.

At the same time, on the GEE platform, there are six input parameters to define RF classifiers: (1) the number of classification trees to create per class, (2) the number of variables per split, (3) the minimum size for a terminal node, (4) the fraction of input to bag per tree, (5) out-of-bag mode, and (6) random seed variable for decision tree construction (https://code.earthengine.google.com/). Breiman (2001) proposed that the overall accuracy of the classifications in the RF algorithm depends on the number of trees, while more decision trees also increase the processing time. Considering the overall accuracy and classification processing duration, we selected the 100 decision trees as the optimum value for this classification, and other parameters were defaults.

The postprocessing of Landsat images mainly included two tasks: vectorization and edge line extraction. The discriminated Landsat images were first vectorized to calculate the salt marsh area, mudflat area, and water area. Subsequently, utilizing the 'canny' operators, we further extracted the edge lines of the salt marshes and mudflats. Finally, we exported all the datasets and images that were required for follow-up statistics. All of the processing procedures were programmed on the GEE platform, which effectively improves remote sensing image processing efficiency.

2.3.3. *Estimates of salt marsh/mudflat area and elevation*

The salt marshes are located are a higher position in the wetland and are rarely submerged by high tide levels, so their areas are minimally affected by tidal level fluctuations (Fig. 3). Therefore, the salt marsh area was directly obtained from the Landsat image interpretation. Subject to Landsat image limitations, continuous time series data with the mudflat-exposed area at low tide levels are challenging to acquire (Jia et al., 2021). Considering that the mudflat-exposed area is sensitive to water level fluctuations, we attempted to explore their relationship (Supplementary Fig. 1). The results indicated that the rating curves between the exposed area and the tidal levels could be well expressed by the 2nd degree polynomial equations, which are as follows:

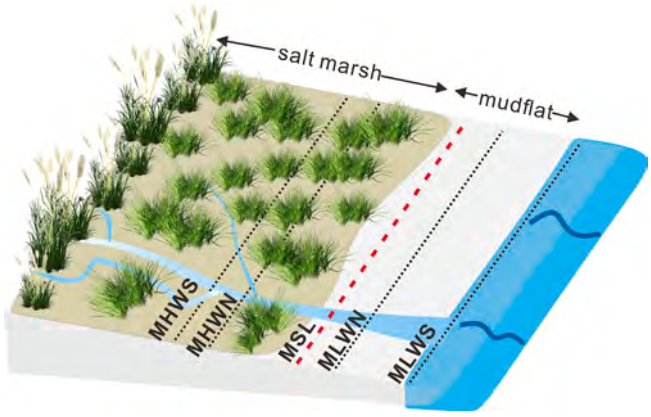

Fig. 3. Schematic of salt marsh and mudflat distributions in the Eastern Chongming wetland. MHWS: mean high water springs; MHWN: mean high-water neaps; MSL: mean sea level; MLWN: mean low water neaps; and MLWS: mean low water springs.

$$s_h = f_n(\mathrm{h}) = \mathrm{a}_n\mathrm{h}^2 + \mathrm{b}_n h + c_n, n = 2002, 2003, \cdots 2019 \quad (5)$$

where h is the tidal level corresponding to Landsat image exposure time and s_h is the exposed area at the corresponding tidal level.a_n,b_n, and c_n present the annual fit coefficients in a specific year, and n represents the specific year. Subsequently, utilizing the quadratic equations, we further calculated the mudflat exposed area at the mean low water spring (MLWS = 0.5 m). The total wetland area (salt marsh area + mudflat area) had a similar connection with the tidal level (Supplementary Fig. 2).

Additionally, according to the relation between the wetland area and tidal levels, salt marsh and mudflat accretion variations from 2002 to 2019 were further recalculated. Here, the original locations of the salt marsh seaward edges with a tide level of 2.75 m and mudflat seaward edges with a tide level of 2.0 m in 2002 were used as the benchmarks for detecting the vertical elevation changes of the salt marshes and mudflats, respectively. The calculated equation can be described as follows:

$$\Delta\mathrm{H} = f_n^{-1}(s_{n+1}) - f_n^{-1}(s_n) \quad (6)$$

$$\mathrm{H}_n = \sum_{2002}^{n}(\Delta\mathrm{H}) \quad (7)$$

where ΔH is the calculated elevation variation based on the previous area of salt marsh/mudflat, s_n is the salt marsh/mudflat area in a specific year, and f_n is the relation formula between tidal level and total wetland area/mudflat area in a specific year. H_n is the accumulated salt marsh elevation variation from the original year of 2002 to 2019.

Notably, the local areas and vertical accumulated changes in the NZ and EZ were also estimated by these equations, whereas SZ was not involved in the calculation due to frequent recessions in this area (Supplementary Figs. 3–6).

2.3.4. Digital shoreline analysis system (DSAS)

The DSAS, a software extension for ArcGIS, provides an automated method for detecting multiple historical shoreline changes (https://code.usgs.gov/cch/dsas). In this study, the edge line changes in the salt marshes and mudflats in the three zones were calculated by the DSAS to indicate the lateral evolution of wetlands. Specifically, the edge lines of the salt marshes and mudflats in 2002 were divided into 200–300 sections with a 50 m distance. Then, the interannual edge line migrations of each transect were automatedly generated by DSAS.

2.3.5. Accuracy assessment

Results are affected by remote sensing resolution and data processing; thus, error analysis is necessary to verify the accuracy of the results (Lawrence and Wrlght, 2001). For the Landsat image classification, error matrices with independent validation samples were employed to assess the performance of the RF classification algorithm (Liu et al., 2016). Producer accuracy, user accuracy, overall accuracy, and kappa coefficient (k) were the four indicators used in this accuracy assessment (Jia et al., 2018). Table 3 shows the annual accuracy assessment for the different land cover types obtained through the RF method using test data, indicating a high level of confidence in the different land cover types of the RF classification in this work. Specifically, the overall annual accuracies ranged between 0.971 and 0.997 for all observation years, and these kappa coefficients were higher than 0.96. Additionally, the three classes of producer and user accuracies were over 0.9, and most of these accuracies were 0.98 (Table 3).

The other deviations occurred based on the original data post-processing, including the fitting curve and elevation calculation. Supplementary Figs. 1 and 2 show the annual fitting curves between the mudflat areas/wetland areas and tidal levels with high correlation, as most of the correlation coefficients of the fitting equations were over 0.95. Considering the deviation of this linear interpolation method, we constructed a 95% confidence interval of our results.

Table 3
Confusion matrix for assessing the performance of the RF machine learning algorithm.

		Water	Salt marsh	Tidal flat	Overall accuracy	Kappa coefficient
2002	Producer accuracy	0.995	1	0.974	0.991	0.988
	User's accuracy	0.973	0.995	0.996		
2003	Producer accuracy	0.991	0.993	0.952	0.979	0.969
	User's accuracy	0.982	0.974	0.986		
2004	Producer accuracy	1	0.991	0.996	0.995	0.993
	User's accuracy	1	0.994	0.987		
2005	Producer accuracy	1	0.993	0.993	0.995	0.993
	User's accuracy	1	0.995	0.989		
2006	Producer accuracy	1	0.991	0.993	0.994	0.991
	User's accuracy	1	0.995	0.986		
2007	Producer accuracy	1	0.993	0.984	0.992	0.988
	User's accuracy	0.991	0.993	0.989		
2008	Producer accuracy	1	0.997	0.989	0.995	0.992
	User's accuracy	1	0.993	0.996		
2009	Producer accuracy	1	0.995	0.967	0.988	0.982
	User's accuracy	0.995	0.979	0.996		
2010	Producer accuracy	1	0.979	0.934	0.971	0.961
	User's accuracy	0.979	0.97	0.965		
2011	Producer accuracy	1	0.988	0.978	0.988	0.981
	User's accuracy	1	0.986	0.981		
2013	Producer accuracy	0.995	0.981	0.941	0.973	0.964
	User's accuracy	0.983	0.968	0.973		
2014	Producer accuracy	1	0.997	0.996	0.997	0.995
	User's accuracy	0.995	1	0.996		
2015	Producer accuracy	1	0.993	0.973	0.988	0.98
	User's accuracy	0.995	0.984	0.989		

(continued on next page)

Table 3 (*continued*)

		Water	Salt marsh	Tidal flat	Overall accuracy	Kappa coefficient
2016	Producer accuracy	1	1	0.989	0.996	0.993
	User's accuracy	0.995	0.995	1		
2017	Producer accuracy	0.995	1	0.993	0.996	0.991
	User's accuracy	0.995	0.995	1		
2018	Producer accuracy	1	0.997	0.993	0.996	0.993
	User's accuracy	0.995	0.997	0.996		
2019	Producer accuracy	0.995	0.962	0.979	0.975	0.969
	User's accuracy	1	0.984	0.943		

3. Results

3.1. Area changes in the salt marshes and mudflats

Fig. 4 shows the annual area changes in the salt marshes and mudflats in the ECW between 2002 and 2019, including the local area variations in the NZ and EZ. The original salt marsh area of the ECW in 2002 was approximately 38 km^2 (Fig. 4). In 2019, this area expanded to 102 km^2, which was nearly three times that in 2002, indicating that the salt marshes of the ECF exhibited a remarkable expansion trend with an increasing rate of 3.818 km^2/yr (Fig. 4A). Similarly, simple trend analyses of the NZ and EZ local areas from 2002 to 2019 also clearly indicated interannual salt marsh expansion with rates of 2.641 km^2/yr and 0.978 km^2/yr, respectively (Fig. 4B). This result reflected that the growth rate of the NZ salt marsh was more significant than that of the EZ salt marsh.

At the same time, the total mudflat area in the ECW mainly fluctuated, with a total area of approximately 84.9 km^2 over the past decades (Fig. 4C). However, the NZ and EZ mudflats displayed opposite development processes from 2002 to 2019. The annual NZ mudflat area has shown a gradually increasing trend with an average growth rate of 0.922 km^2/yr, whereas the EZ mudflat has presented a slightly decreasing trend. The mudflat erosion rate in the EZ reached 0.738 km^2/yr (Fig. 4D).

3.2. Lateral migration of salt marshes and mudflats

The migrations of salt marshes and mudflat margins effectively reveal their lateral changes (Fagherazzi et al., 2020). Intuitively, the salt marshes and mudflats in the ECW exhibited gradual seaward movements (Supplementary Fig. 7). Fig. 5 shows the salt marsh and mudflat lateral migrations during 2002–2019 in the three different zones. Specifically, the NZ salt marsh was a rapid deposition area with annual seaward expansion rates of 60.6 m/yr. The NZ mudflat displayed more significant expansion than the salt marsh, with an average seaward migration rate of 103.7 m/yr (Fig. 5A). The total migration distances of the NZ salt marshes and mudflats were over 1000 m and 1700 m, respectively, between 2002 and 2019. Moreover, similar lateral migrations of salt marshes and mudflats were detected in the EZ (Fig. 5B); the salt marshes had a seaward expansion rate of 39.5 m/yr, and the mudflats had a rate of 36 m/yr. The expansion rate of the mudflats was slightly slower than that of the salt marshes. Despite the widespread expansion of wetlands in the NZ and EZ, the SZ wetlands showed a slight landward retreat (Fig. 5C). The annual recession rates of salt marshes and mudflats in the SZ were 18.5 m/yr and 13.3 m/yr, respectively.

Furthermore, the mudflats were divided into four areas: the

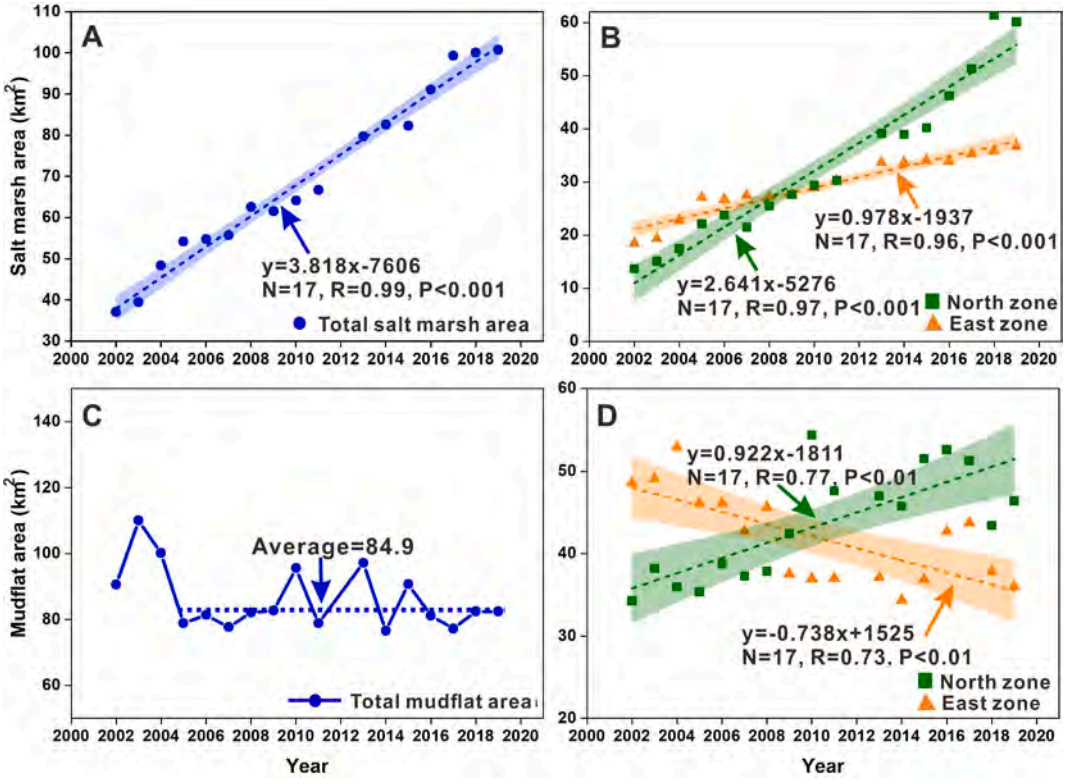

Fig. 4. Annual salt marsh and mudflat area variations from 2002 to 2019. A. Total salt marsh area; B. NZ and EZ salt marsh areas; C. total mudflat area; D. NZ and EZ mudflat areas.

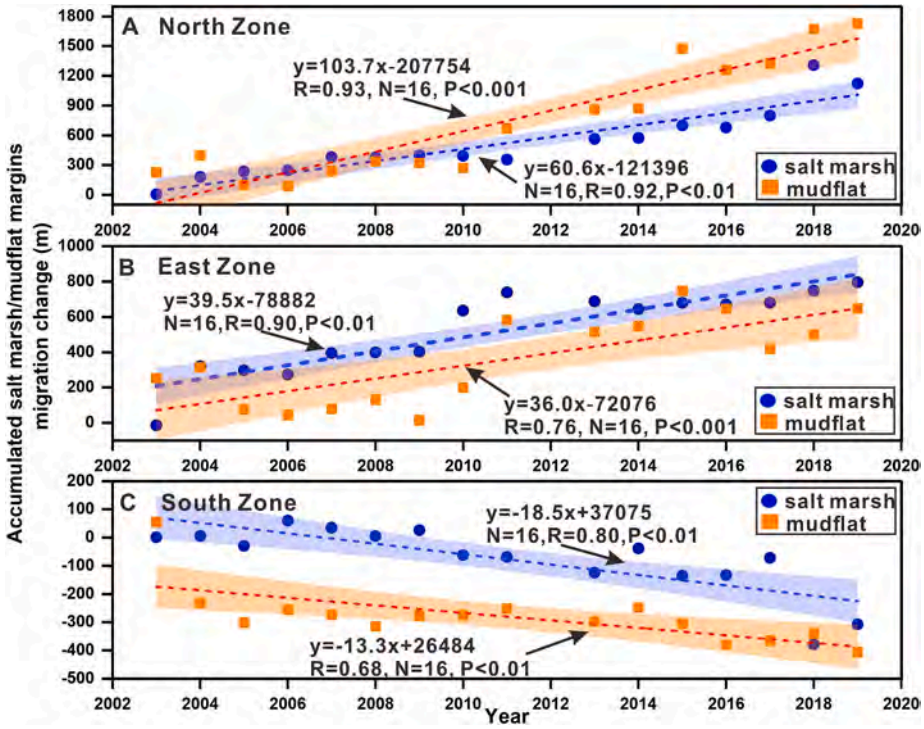

Fig. 5. Annual salt marsh and mudflat margin migrations from 2002 to 2019 in different zones; A. north zone; B. east zone; and C. south zone.

southeastern area, the eastern area, the northeastern Area, and the northern area. The width of the northern area mudflats significantly increased after 2005, while the widths of the other three mudflat areas exhibited fluctuations over the years (Fig. 6A, 6B). Fig. 6C indicates that the annual decrease rates of mudflat widths in the southeastern area and eastern area reached 26.9 m/yr and 21 m/yr, respectively. At the same time, the mudflat widths of the northeastern area and northeastern area gradually expanded from 2002 to 2019 at 30.5 m/yr and 49.9 m/yr, respectively (Fig. 6C). Overall, the mudflats exhibited explicit, distinct variations that changed from sediment erosion to deposition from south to north.

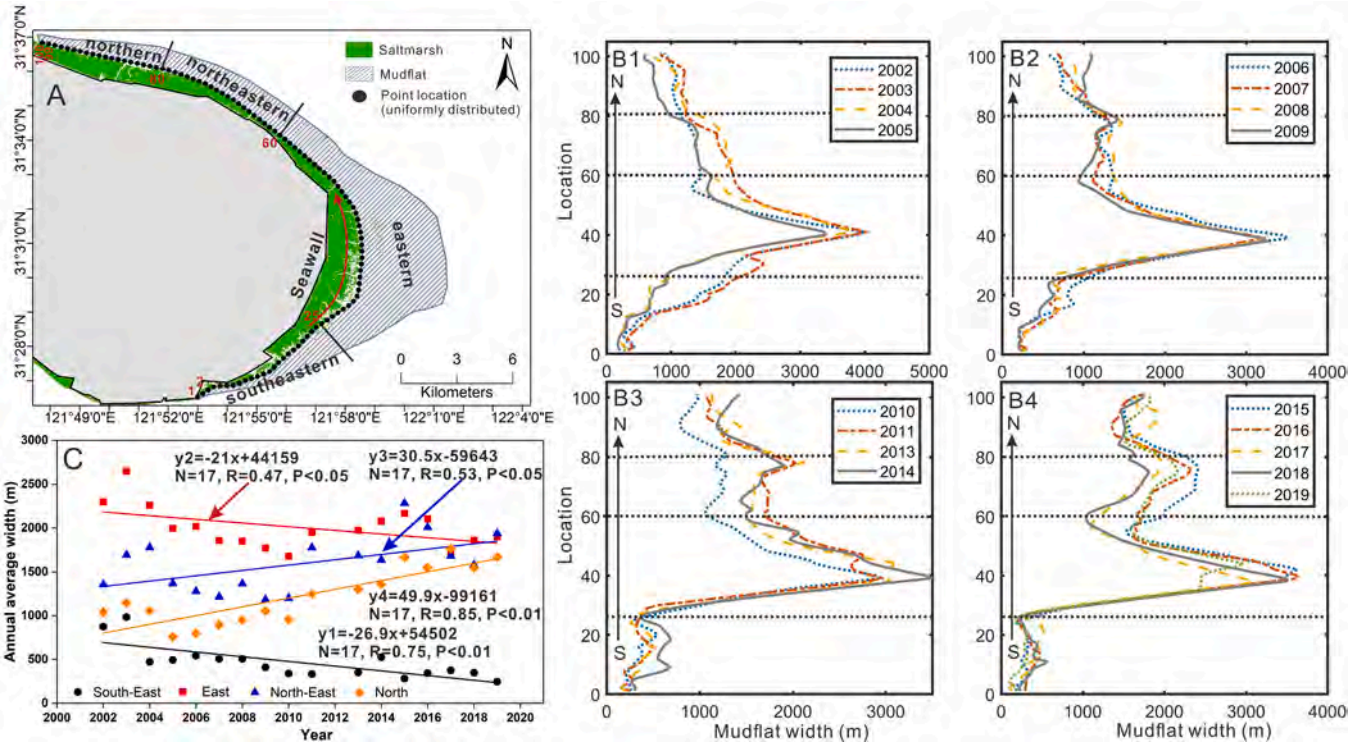

Fig. 6. Mudflat width variations during 2002–2019. A. The locations and serial numbers of transects; B. annual mudflat width of different transects; and C. annual average width statistics for the different zones.

3.3. Elevation changes in the salt marshes and mudflats

Elevation changes are imperative indicators of salt marsh and mudflat morphodynamics. The NZ salt marshes and mudflats presented significant accretion trends, with significant levels reaching 0.97 and 0.95 during 2002–2019, respectively. The accumulated elevation changes in the salt marshes reached almost 3 m from 2002 to 2019, and the average annual elevation change rate was 0.178 m/yr (Fig. 7A). Additionally, the mudflat deposition in the NZ was higher than that of the salt marsh, which had an accretion rate of 0.256 m/yr (Fig. 7A).

In the EZ, the accretion rates were reduced significantly. Between 2004 and 2008, the EZ salt marsh elevation changes occurred due to erosion. Subsequently, the gradual deposition trend recovered after 2008, with an annual increase of 0.103 m/yr (Fig. 7B). The accumulated salt marsh elevation increased by approximately 1 m in the past decade. Moreover, the EZ mudflat exhibited a similar elevation evolution process. Nevertheless, its accretion was much lower, with an average accumulation of 0.066 m/yr from 2005 to 2019 (Fig. 7B). These results indicate that of the wetlands, the NZ wetlands had the most remarkable accretion zone with the maximum lateral migration and vertical deposition rates.

4. Discussion

4.1. Sediment supply

Tidal flat morphodynamics are controlled by a combination of influences, such as tidal range, relative SLR, marsh elevation within the tidal frame, and sediment source supply (Lovelock et al. 2015; Kirwan et al., 2016; Crosby et al., 2016).

A sufficient sediment supply is one of the important drivers supporting salt marsh and mudflat growth (Fagherazzi et al., 2020). The ECW has multiple sediment sources, including fluvial sediment and longshore sediment transport (Yang et al., 2020; Leonardi et al., 2021). Fig. 8A indicates that the fluvial suspended sediment load at the Datong station had a sharply decreasing trend (27.99×10^6 t/yr) between 2003 and 2008 because of TGD operations (Dai et al., 2016b), even though the discharge remained almost unchanged (Fig. 8A). Moreover, between 2008 and 2019, the SSD was relatively stable at a mean of approximately 121.4×10^6 t/yr (Fig. 8A). Obviously, the SSD reduction still induced the expansion of the salt marshes and mudflats in the ECW, which could be seen from the negative relationship between them (Fig. 8B). Nevertheless, a short-term vertical decreasing trend occurred in the EZ salt marshes and mudflats from 2003 to 2008 (Fig. 7B), which was attributable to the decreasing fluvial SSD. Although the fluvial SSD reduction had little impact on ECW development in the long term, it hampered local mudflat expansion.

Fig. 8C reveals that the annual SSC in the estuary at Sheshan station, near the ECW, was approximately 0.77 kg/m^3 from 2009 to 2017, and this value remained almost unchanged (Fig. 8C). This result explicitly demonstrates that even if the fluvial sediment underwent a sharp decline, the constant local SSC could still support salt marsh development. This finding is in line with the theory that sediment availability is the critical factor controlling salt marsh expansion and survival (Fagherazzi et al., 2020).

4.2. Effects of local conditions

An estuary's regional morphology significantly affects sediment transport dynamics and wetland evolution (Dai et al., 2018a; Dai, 2021). The ECW is located in a complex tidal environment. Its NZ is near the North Branch of the CJD, and its SZ is near the North Channel. Limited by the regional morphology, the North Branch only receives 1% of the runoff flows from the Changjiang River but accepts 25% of the total tidal prism (Chen and Chen, 2003). As a flood-dominated channel, it is primarily controlled by estuarine hydrodynamics and mainly receives sediment from the sea (Dai et al., 2016a). At the same time, the mouth of the North Branch is recognized as one of the highest SSC zones in the CJD, and a substantial amount of sediment is deposited in this area (Dai et al., 2018b). Therefore, flood-dominated hydrodynamics and sufficient sediment supply are responsible for promoting northern and eastern wetland deposition (Leonardi et al., 2021; Dai, 2021) (Fig. 9A).

In contrast to the North Branch, the North Channel is dominated by the ebb tide-dominated current (Mei et al., 2018). The SZ is constrained by strong hydrodynamic conditions between the flood-dominated channel and ebb-dominated channel and thus faces a large obstruction to expansion (Fig. 9A). In addition, waves in Sheshan generally are in southern or southeastern directions in spring and summer and northern or northeastern directions in autumn and winter (Yun, 2004; Wu and Zhu, 2010) (Fig. 9B). The southerly wave directly erodes the mudflats of the SZ in the ECW due to the open surrounding sea areas. Therefore, the field measurement results displayed the highest slope in the SZ at 1%, and the EZ and NZ slopes were 0.08% and 0.1%, respectively (Yang et al., 2002), which could be attributed to the local actions of tidal currents and wind-driven waves. In addition, the ebb-dominated circumstances in the North Channel carry the sediment away from the tidal flats (Wu and Zhu, 2010; Liu et al., 2020). The strong hydrodynamic environment and insufficient sediment supply are remarkable obstructions to SZ expansion. On the other hand, the SZ has a steep slope and narrow mudflat distribution and is unable to withstand wave and tide current dynamics, which force the mudflats to erode and become steeper. From this increase in slope steepness, the margin between the salt marsh and mudflat platforms becomes increasingly unstable. Eventually, this process leads to salt marsh retreat and landward

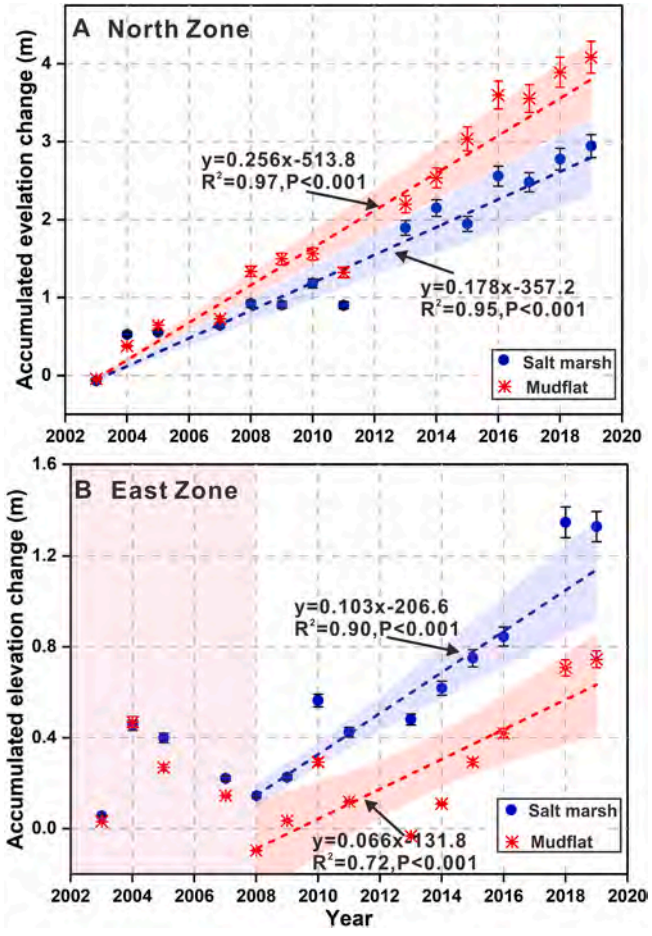

Fig. 7. Accumulated elevation changes in the salt marshes and mudflats in the NZ and EZ from 2002 to 2019.

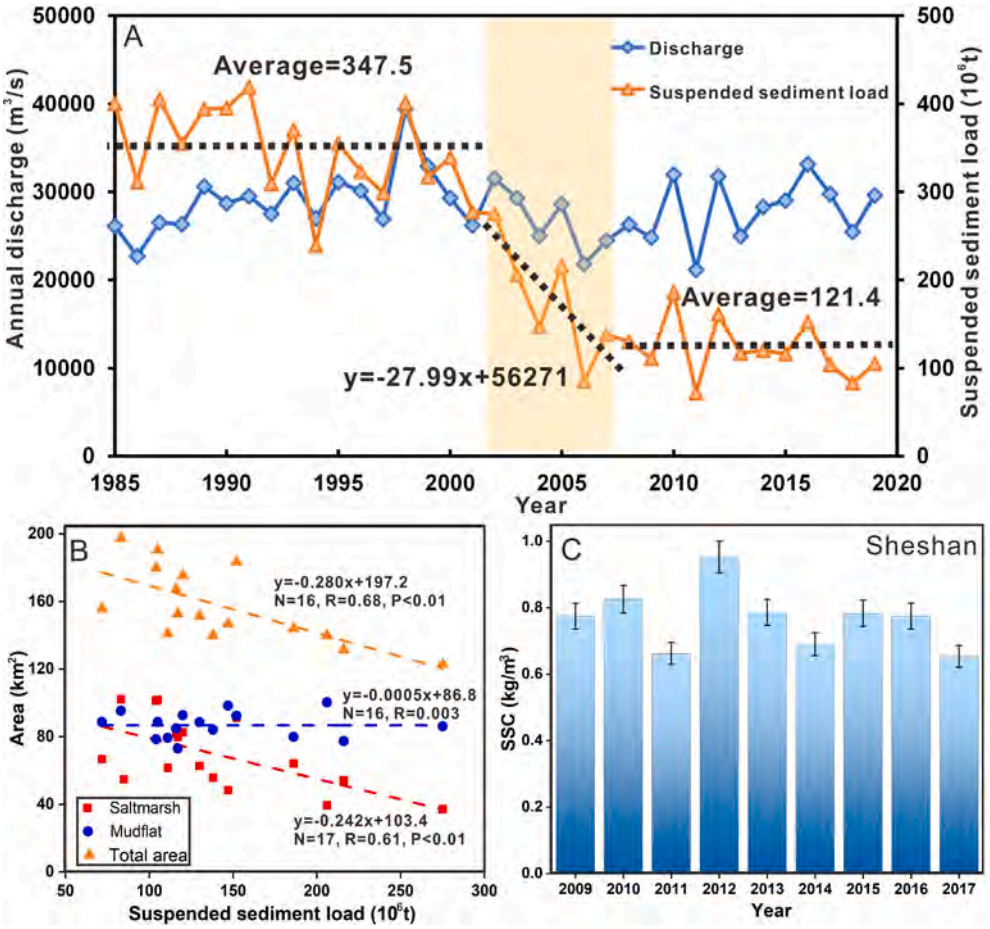

Fig. 8. A. Annual variations in discharge and suspended sediment load at Datong station from 1985 to 2019. B. The relations between salt marsh/mudflat areas and the fluvial sediment load; C. the annual suspended sediment concentrations at Sheshan station from 2009 to 2017 (the data are from (Yang et al., 2020)).

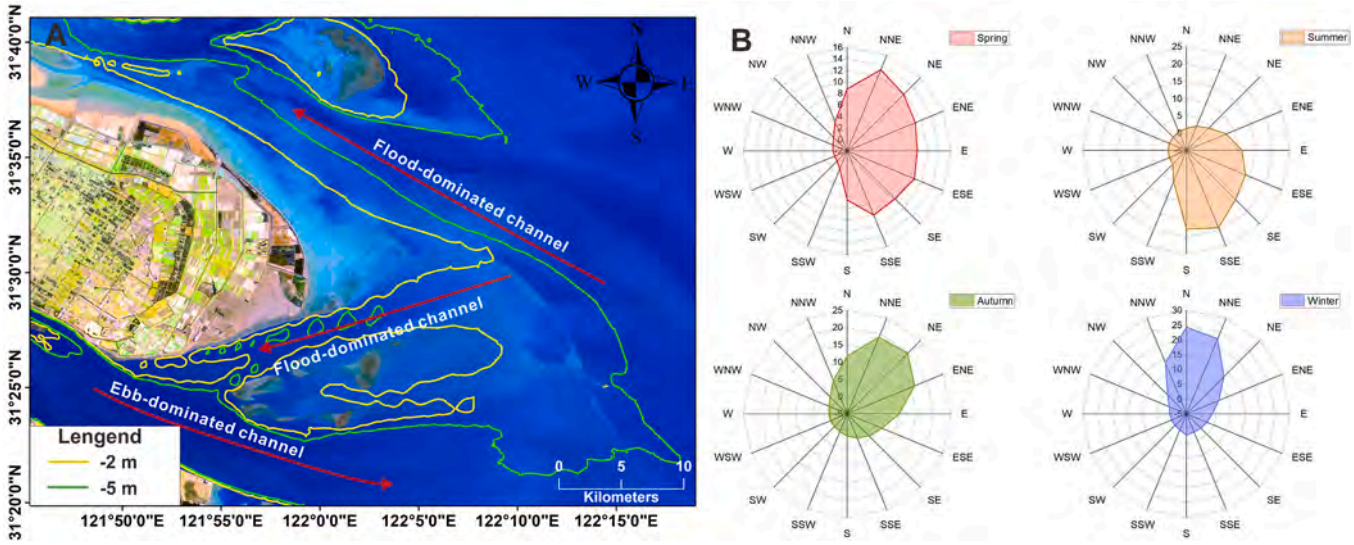

Fig. 9. A. Divergence of flood and ebb currents in the surrounding areas of the Eastern Chongming Wetland; B. the seasonal wave direction distributions at Sheshan station.

migration (van de Koppel et al., 2004).

4.3. Sea-level rise

Existing knowledge reveals that the sustainability of wetlands is now severely threatened by the increase in SLR due to global climate change (Rizzetto and Tosi 2011; Kirwan and Megonigal, 2013; Linhoss et al., 2015). Globally, many studies have demonstrated that marsh-mudflat ecosystems are in danger of disappearing if they cannot accrete elevation at rates that match SLR (Lovelock et al. 2015; Crosby et al., 2016).

One crucial index assessing salt marsh vulnerability is that which compares salt marsh surface elevation changes with regional sea-level variations (Horton et al., 2018). Recent research has indicated that the rate of global mean SLR presents an accelerating trend, with a rate that increased from 1.4 mm/yr in 1880–1993 to 2.9 mm/yr in 1993–2010 (Church and White 2011). In addition, influenced by the high forcing and unfavorable ice sheet dynamics, the SLR might exceed 2 m in many regions (Kopp et al., 2017).

Here, we assessed the relative SLR in the CJD (using the theoretical minimum tidal surface as the benchmark). The mean sea level in the CJD exhibited an increasing trend with an increasing rate of 4.7 mm/yr, despite the interannual fluctuations (Fig. 10). Furthermore, Wang (2010) determined that the subsidence rate in the ECW was approximately 5.2 mm/yr in recent years. Therefore, the relative SLR is approximately 9.9 mm/yr because of the mean SLR and subsidence rate coupling effects. Based on the results related to salt marsh and mudflat accretions, we found that the annual accretion in the EZ mudflat was 66 mm/yr, excluding the SZ erosion (Fig. 7). Nevertheless, the local wetland subsidence process, including sediment compaction and organic matter decomposition, are not considered here in this remote sensing technology. It is notable that although the local wetland subsidence process could have contributed to lowering the rates of elevation change, subsidence rates were much smaller than the ECW accretion rate. Yang et al. (2020) also proposed an accretion rate of 33–49 mm/yr in the ECW. Although the estimated annual accretion rate was greater than that in the previous study proposed by Yang et al. (2020), it could be concluded that the enhancement of the salt marshes in the ECW was remarkably higher than the relative SLR in the ECW, reflecting that these areas are sufficiently resilient to the SLR threat.

4.4. Effects of human intervention

In the ECW, a series of artificial projects, including embankment construction and vegetation plantations, have been conducted in recent decades to accelerate marsh sedimentation (Luo et al., 2017). Fig. 11 shows that several large-scale reclamation projects were constructed in the ECW during 1999–2019. The embankments interrupted the tidal current, decreased the water flow velocity, and restricted the sediment-carrying capacity, thus accelerating wetland sedimentation (Li et al., 2011). Subsequently, Lu and Jiang (2013) also identified that the ECW underwent a remarkable expansion in the first three years following the construction of the embankments in 1999 and then gradually recovered to equilibrium conditions. The results indicate that mudflat areas in 2002–2003, 2010, 2013, and 2015 appeared to increase (Fig. 4C), which confirms that these projects dramatically promoted mudflat expansion in the following 1–2 years (Fig. 11).

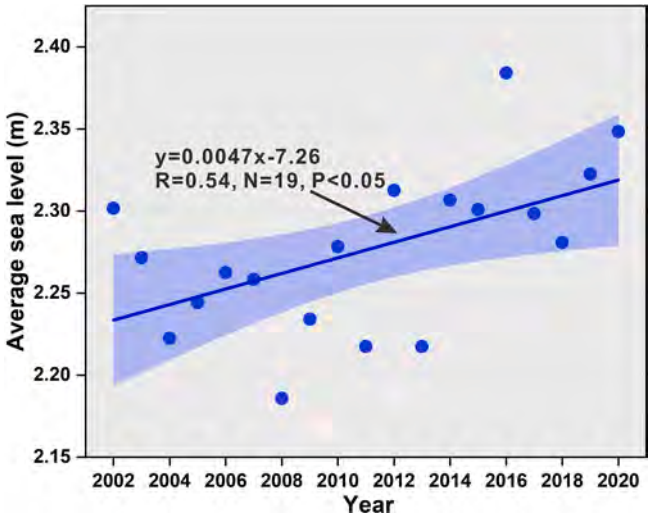

Fig. 10. Annual sea levels at the Hengsha tidal station between 2002 and 2019, and the elevation datum are the theoretical minimum tidal surfaces.

Additionally, with their immense capacity for diminishing flow velocity and trapping sediment, salt marsh vegetation is considered one of the driving factors of wetland development (Kirwan and Megonigal, 2013). Therefore, *Spartina alterniflora* was artificially introduced in 2001 and 2003 to promote the development and stability of the ECW (Han et al., 2009). Furthermore, the cultivation of *Spartina alterniflora* in the ECW expanded from 33 ha in 2000 to 916 ± 131 ha in 2008, *Phragmites australis* increased to 206 ± 25 ha, and *Scirpus mariqueter* decreased from 1660 ha to 963 ± 137 ha from 2000 to 2008 (Ge et al., 2015a). Because of its prominent competitive advantage, *Spartina alterniflora* rapidly spread and became an invasive grass species in the Chongming wetland, resulting in part of the mudflat areas in the ECW being occupied by salt marshes (Ge et al., 2015a; Ge et al., 2015b). Eventually, the ECW reached an equilibrium state, in which the salt marshes continuously expanded and the mudflats remained stable from 2002 to 2019.

Another effect of ECW evolution is the distribution of salt marsh vegetation (Zhang et al., 2020). Based on remote sensing technology, Liu et al. (2020) indicated that the invasive species *Spartina alterniflora* is mainly distributed in the northern and northeastern ECW, while the native species *Scirpus mariqueter* and *Phragmites australis* are in the eastern and southern ECW. Obviously, as a result of its stronger competitive capacity and wider ecological niche, the *Spartina alterniflora* has higher expansion rates than those of the native species (Huang et al., 2007; Zhu et al., 2012). On the other hand, through field measurements, Li and Yang (2009) found that the annual sediment trapping rate of *Spartina alterniflora* was 220.6 ± 172.7 g/m^2 in the CJD, which was remarkably higher than that of *Phragmites australis* (64.9 ± 38.1 g/m^2) and *Scirpus mariqueter* (31.6 ± 10.0 g/m^2). This scenario also explains the generation of differences in the NZ and EZ.

4.5. Dynamic spatial patterns of the salt marshes and mudflats

The three zones of the ECW showed different salt marsh and mudflat dynamics from 2002 to 2019, corresponding to three evolution spatial patterns (Fig. 12). Generally, salt marsh and mudflat development presented similar spatial evolution patterns with deposition in the northern and eastern areas and erosion in the south area (Fig. 12). Specifically, both the NZ salt marshes and mudflats were in a rapid expansion stage. In comparison to salt marsh accretion, mudflat accretion was much higher, including lateral expansions and vertical accumulations (Fig. 12A). The EZ salt marsh and mudflat dynamics experienced stable progradation processes from 2002 to 2019. The lateral expansion rates of the salt marshes and mudflats were similar, while the vertical mudflat deposition was slightly weaker than that of the salt marshes (Fig. 12B). In contrast, the SZ salt marshes and mudflats continuously eroded, which gradually induced their edges to retreat landward (Fig. 12C). Thus, this dynamic could be identified as a slight erosion spatial pattern.

Such spatial patterns reasonably summarize the salt marsh development dynamics. To analyze the external contributors, salt marsh progradation could be linked to the sediment budget of the entire wetland (Ganju et al., 2017). Sufficient sediment and moderate hydrodynamics are prerequisites for marsh progradation, such as in the NZ salt marsh. Otherwise, a marsh would risk retreat, which is similar to that which occurred in the SZ salt marsh. Based on internal mechanisms, there is a potential balance between salt marsh and mudflat. The salt marshes continuously occupied the mudflat areas and forced the mudflat margins to migrate seaward. At the same time, the mudflat seaward expansion also provided the salt marsh greater area to further accelerate salt marsh growth. Conversely, mudflat erosion would have restricted salt marsh development due to a lack of space for expansion.

Furthermore, based on the salt marsh dynamic models proposed by Fagherazzi et al. (2020), this study further forecasts the fate of the ECW in the future. Notably, in the NZ, the mudflats have a higher deposition

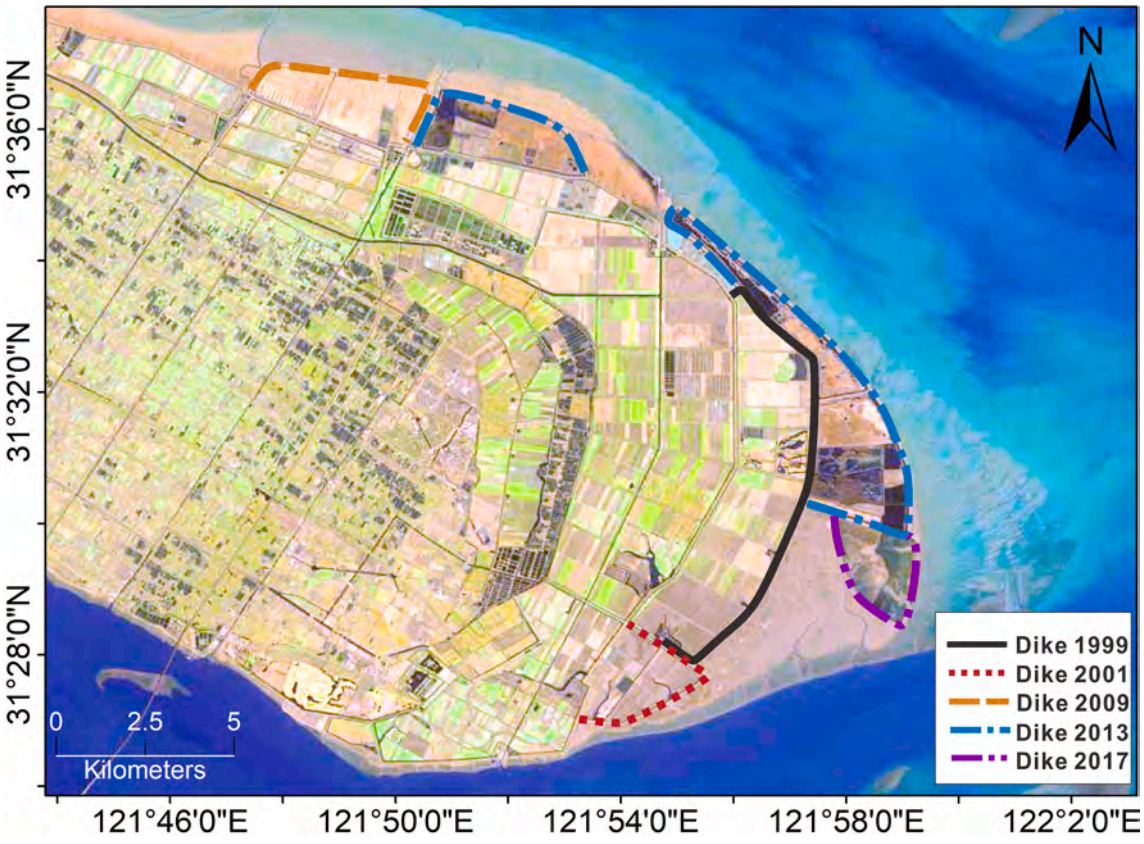

Fig. 11. Locations of embankment constructions in the ECW from 1999 to 2019.

rate than the salt marshes, providing enough space for salt marsh progradation. Nevertheless, mudflat progradation will be limited by the local morphology and hydrodynamics and eventually reach a dynamic balance. Then, mudflats will feedback the salt marshes, affecting their continual progradation and even causing them to retreat. However, in the EZ, the seaward migration and accretion of the salt marshes were greater than those of its adjacent mudflat, and the mudflats were in the erosion stage. Although the large mudflat area in the EZ offered sufficient space for salt marsh progradation, the slow accretion of the mudflats would likely gradually increase wave and tide flow impacts and restrict marsh development. In addition, impacted by wave hydrodynamics, the SZ salt marshes and mudflats have experienced landward retreat, which increases the risk of coastal erosion.

4.6. Uncertainty analysis

Multiple remote sensing images and measured tidal levels were combined to build annual fitted linear equations, and this method effectively exhibited the long-term and successive morphological evolution of the EDW. Nevertheless, there are still some uncertainties in this measurement, including data source errors and processing errors. Specifically, the data source error primarily refers to the 30 m spatial resolution of Landsat images, which would induce a pixel error of $9X10^{-4}$ km^2. Therefore, selecting a large study area is a precondition for decreasing this data source error (Okin and Gu, 2015). The results show that the EDW area is over 100 km^2, remarkably larger than the pixel error, which would effectively decrease the impact from the data source error. At the same time, although we utilized the measured tidal level to construct the relationship between the tidal flat areas and tidal levels, due to the topographic influence, the tidal levels in the different regions of the EDW were not entirely consistent at the same moment. This scenario affected the statistical relations between areas and tidal levels and then further influenced tidal flat area acquisition. Although the annual fitting curves between the tidal flat areas and tidal levels had high correlation coefficients ($R^2 > 0.95$), deviations remained between the fitted tidal flat areas and the actual values.

Overall, compared with the results from the few and intermittent Landsat images, the results from numerous and serial Landsat images applied through machine learning provided increased accuracy and decreased randomness. This method can precisely describe the morphological evolution process in the ECW in recent decades. Furthermore, this work also demonstrated the long-term interaction of vegetation-geomorphology between salt marshes and mudflats in the ECW, which is difficult to detect through episodic field measurements.

5. Conclusion

Influenced by SLR and fluvial SSD reduction, most of the salt marshes in mega-deltas are under tremendous pressure. To better protect and manage these precious natural resources, it is essential to detect the long-term morphodynamics of salt marshes and demonstrate the variability in salt marsh and mudflat evolution and their underlying connections. Taking the ECW as an example, this paper proposed a creative method to detect salt marsh and mudflat multidimensional development by combining a full-time series of remote sensing images and regional tidal elevations. The main conclusions are as follows:.

1. The whole Eastern Chongming wetland was experiencing deposition, even though there were distinct changes in the local salt marshes. Between 2002 and 2019, the northern salt marshes and mudflats of the Eastern Chongming wetland exhibited remarkable expansions, and their areas increased 2.64 km^2/yr and 0.922 km^2/yr, respectively, with seaward migrations and accretions. The eastern salt marshes had moderate progradation with lateral changes of 39.5 m/yr and vertical increases of 0.103 m/yr, whereas the mudflats experienced slight erosion with an area reduction of −0.738 km^2/yr.

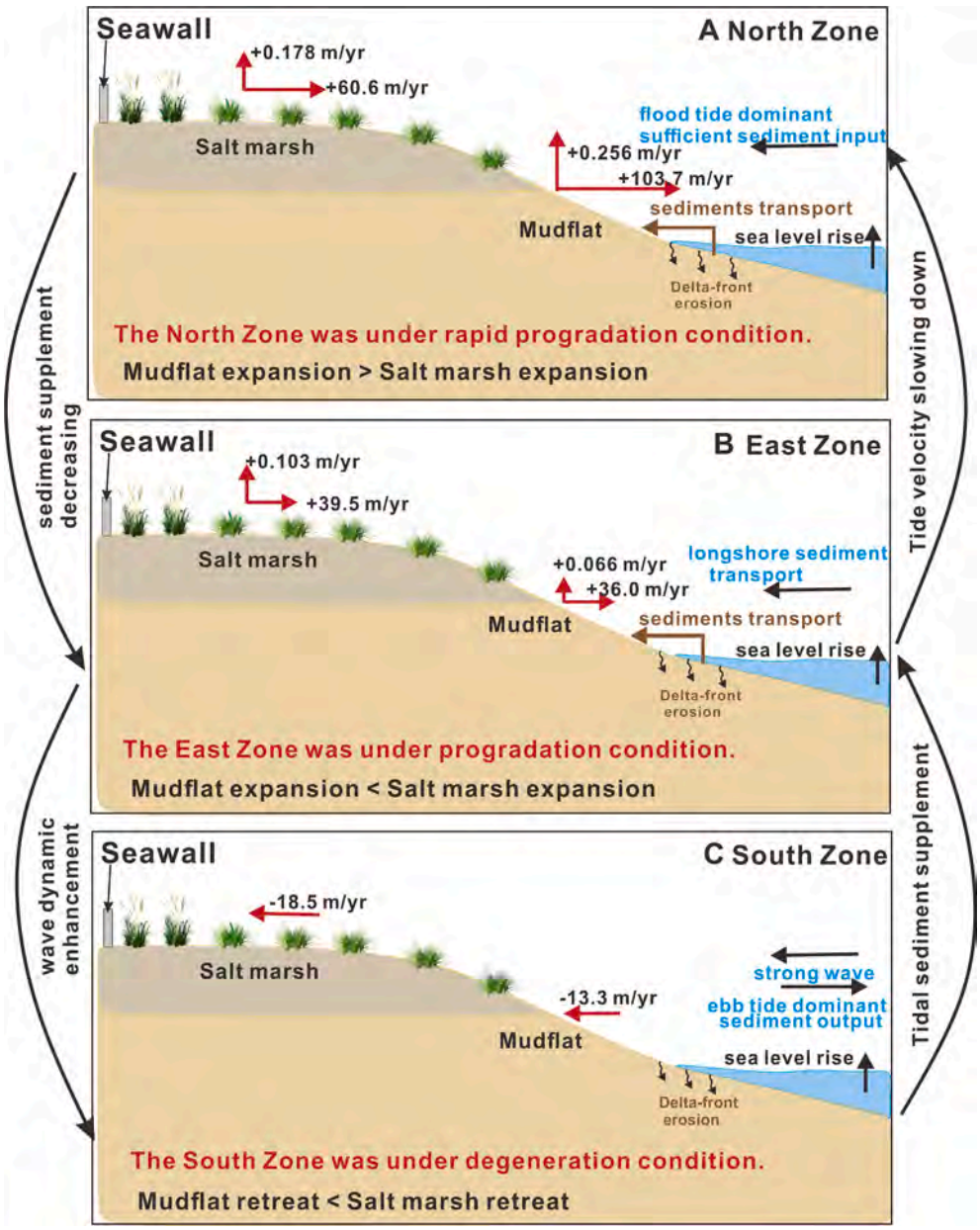

Fig. 12. Three patterns of salt marsh and mudflat dynamics.

Nevertheless, landward retreats were detected in the SZ salt marshes and mudflats.

2. Fluvial SSD is not a dominant factor controlling salt marsh development, while the high local SSC ensured salt marsh progression in the Eastern Chongming wetland. At the same time, the relative sea-level rise in the Eastern Chongming wetland was lower than the salt marsh and mudflat accretions, providing sufficient wetland resilience to sea-level rise. Local hydrology, human intervention, and vegetation effects are recognized as the primary factors that impact the spatial evolution pattern of salt marshes and mudflats.
3. The salt marsh and mudflat dynamics in the Eastern Chongming wetland were divided into three patterns. The first pattern is the rapid expansion pattern of the salt marshes in the western zone, which are supported by sufficient sediment and weaker hydrodynamics. The second pattern is the moderate progradation pattern of salt marshes in the eastern zone. Although seaward migration of the salt marshes occurred, the mudflats faced minimal erosion. The third pattern is the slight erosion pattern of the salt marshes in the western zone. Landward migration of the salt marshes and mudflats revealed recession of the salt marsh system.

CRediT authorship contribution statement

Yaying Lou: Writing – original draft, Data collection and analysis. **Zhijun Dai:** Ideal conception, Writing, Review & editing. **Chuqi Long:** Data curation. **Hui Dong:** partly discussion. **Wen Wei:** partly data collection. **Zhenming Ge:** partly discussion and data analysis.

Declaration of Competing Interest

The authors declare that they have no known competing financial interests or personal relationships that could have appeared to influence the work reported in this paper.

Acknowledgments

This research presented was supported by the Joint Key Funds of National Natural Science Foundation of China (U2040202), Key Projects of Intergovernmental Science and Technology Innovation Cooperation of the Ministry of Science and Technology in China (2018YFE0109900), the Shanghai International Science and Technology Cooperation Fund Project (19230712400), and the Academic Capacity Improvement Program for Outstanding Doctoral Students of East China Normal University (40500-20102-222000/003/006). The authors would like to thank Editor Marco Borga, Associate Editor, and the other two anonymous reviewers for several constructive comments that have helped the substantial improvement of the manuscript.

Appendix A. Supplementary data

Supplementary data to this article can be found online at https://doi.org/10.1016/j.jhydrol.2022.127681.

References

Allen, J.R., 2000. Morphodynamics of Holocene salt marshes: a review sketch from the Atlantic and Southern North Sea coasts of Europe. Quat. Sci. Rev. 19 (12), 1155–1231.

Anthony, E.J., Brunier, G., Besset, M., Goichot, M., Dussouillez, P., Nguyen, V.L., 2015. Linking rapid erosion of the Mekong River delta to human activities. Sci. Rep. 5 (1), 1–12.

Anthony, E.J., Dobroniak, C., 2000. Erosion and recycling of estuary-mouth dunes in a rapidly infilling macrotidal estuary, the Authie, Picardy, northern France. Special Publications of the Geological Society of London 175, 109–121.

Barbier, E.B., Koch, E.W., Silliman, B.R., Hacker, S.D., Wolanski, E., Primavera, J., Stoms, D.M., 2008. Coastal ecosystem-based management with nonlinear ecological functions and values. Science 319 (5861), 321–323.

Barbier, E.B., Hacker, S.D., Kennedy, C., Koch, E.W., Stier, A.C., Silliman, B.R., 2011. The value of estuarine and coastal ecosystem services. Ecol. Monogr. 81 (2), 169–193.

Breiman, L., 2001. Random Forests. Machine Learning 45, 5–32.

Carlin, J.A., Dellapenna, T.M., 2014. Event-driven deltaic sedimentation on a low-gradient, low-energy shelf: The Brazos River subaqueous delta, northwestern Gulf of Mexico. Mar. Geol. 353, 21–30.

Carniello, L., Defina, A., D'Alpaos, L., 2009. Morphological evolution of the Venice lagoon: evidence from the past and trend for the future. J. Geophys. Res. Earth Surf. 114 (F4), F04002.

Chen, J.Y., Chen, S.L., 2003. The changes of ecologic environment in Yangtze River estuary and some suggestions for estuary regulation. Water Resource and Hydropower. Engineering 34 (1), 19–25 in Chinese, with English abstract.

Chen, S. l., Zhang, G. A., Yang, S. L., Yu, Z. Y., (2004). Temporal and Spatial Changes of Suspended Sediment Concentration and Resuspension in the Yangtze River Estuary and Its Adjacent Waters. Acta Geographica Sinica, 59(2), 261-264. (In Chinese with English Abstract).

Chen, B., Xiao, X., Li, X., Pan, L., Doughty, R., Ma, J., Dong, J., Qin, Y., Zhao, B., Wu, Z., Sun, R., Lan, G., Xie, G., Clinton, N., Giri, C., 2017. A mangrove forest map of China in 2015: Analysis of time series Landsat 7/8 and Sentinel-1A imagery in Google Earth Engine cloud computing platform. ISPRS J. Photogramm. Remote Sens. 131, 104–120.

Chen, J.Y., Zhu, H.F., Dong, Y.F., Sun, J.M., 1985. Development of the Changjiang estuary and its submerged delta. Cont. Shelf Res. 4 (1–2), 47–56.

Church, J.A., White, N.J., 2011. Sea-level rise from the late 19th to the early 21st century. Surv. Geophys. 32 (4-5), 585–602.

Costanza, R. (2006). Nature: ecosystems without commodifying them. Nature, 443, 749.

Crosby, S.C., Sax, D.F., Palmer, M.E., Booth, H.S., Deegan, L.A., Bertness, M.D., Leslie, H. M., 2016. Salt marsh persistence is threatened by predicted sea-level rise. Estuar. Coast. Shelf Sci. 181, 93–99.

Dai, Z. J., (2021). Changjiang riverine and estuarine hydro-morphodynamic processes, In the Context of Anthropocene Era. Springer Press.

Dai, Z.J., Liu, J.T., Fu, G., Xie, H.L., 2013a. A thirteen-year record of bathymetric changes in the north passage, Changjiang (Yangtze) estuary. Geomorphology 187 (4), 101–107.

Dai, Z.J., Chu, A., Li, W.H., Li, J.F., Wu, H.L., 2013b. Has suspended sediment concentration near the mouth bar of the Yangtze (Changjiang) estuary been declining in recent years? J. Coastal Res. 289 (4), 809–818.

Dai, Z., Fagherazzi, S., Mei, X., Chen, J., Meng, Y.i., 2016a. Linking the infilling of the North Branch in the Changjiang (Yangtze) estuary to anthropogenic activities from 1958 to 2013. Mar. Geol. 379, 1–12.

Dai, Z., Fagherazzi, S., Mei, X., Gao, J., 2016b. Decline in suspended sediment concentration delivered by the Changjiang (Yangtze) River into the East China Sea between 1956 and 2013. Geomorphology 268, 123–132.

Dai, Z.J., Liu, J.T., Wei, W., Chen, J., 2014. Detection of the Three Gorges Dam influence on the Changjiang (Yangtze River) submerged delta. Sci. Rep. 4 (6600), 1–7.

Dai, Z., Mei, X., Darby, S.E., Lou, Y., Li, W., 2018a. Fluvial sediment transfer in the Changjiang (Yangtze) river-estuary depositional system. J. Hydrol. 566, 719–734.

Dai, Z., Fagherazzi, S., Gao, S., Mei, X., Ge, Z., Wei, W., 2018b. Scaling properties of estuarine beaches. Mar. Geol. 404, 130–136.

Fagherazzi, S., Mariotti, G., Leonardi, N., Canestrelli, A., Nardin, W., & Kearney, W. S. (2020). Salt marsh dynamics in a period of accelerated sea level rise. Journal of Geophysical Research: Earth Surface, 125, e2019JF005200.

Ganju, N.K., Defne, Z., Kirwan, M.L., Fagherazzi, S., D'Alpaos, A., Carniello, L., 2017. Spatially integrative metrics reveal hidden vulnerability of microtidal salt marshes. Nat. Commun. 8, 14156.

Ge, Z.-M., Zhang, L.-Q., Yuan, L., 2015a. Spatiotemporal dynamics of salt marsh vegetation regulated by plant invasion and abiotic processes in the yangtze estuary: observations with a modeling approach. Estuaries Coasts 38 (1), 310–324.

Ge, Z.-M., Cao, H.-B., Cui, L.-F., Zhao, B., Zhang, L.-Q., 2015b. Future vegetation patterns and primary production in the coastal wetlands of East China under sea level rise, sediment reduction, and saltwater intrusion. J. Geophys. Res. Biogeosci. 120 (10), 1923–1940.

Gu, J., Luo, M., Zhang, X., Christakos, G., Agusti, S., Duarte, C.M., Wu, J., 2018. Losses of salt marsh in china: trends, threats and management. Estuar. Coast. Shelf Sci. 214, 98–109.

Han, Z., Liu, Y., Yun. C. X., Zheng, J. H. (2009). The temporal and spatial dynamics research of vegetation community on Chongming Eastern Beach based on RS and GIS. Proceeding of the 14th China Oceanic Engineering Symposium, 1159-1163. (In Chinese with English abstract).

Horton, B.P., Ian, S., Bradley, S.L., Niamh, C., Matthew, K., Kopp, R.E., et al., 2018. Predicting marsh vulnerability to sea-level rise using Holocene relative sea-level data. Nat. Commun. 9 (1), 2687–2695.

Huang, Y., Sun, W., Zhang, W.E.N., Yu, Y., Su, Y., Song, C., 2010. Marshland conversion to cropland in northeast China from 1950 to 2000 reduced the greenhouse effect. Glob. Change Biol. 16 (2), 680–695.

Huang, H.M., Zhang, L.Q., Yuan, L., 2007. The spatio-temporal dynamics of saltmarsh vegetation for Chongming Dongtan National Nature Reserve, Shanghai. Acta Ecologica Sinica 27, 4166–4172. In Chinese with English Abstract.

Huete, A., Didan, K., Miura, T., Rodriguez, E.P., Gao, X., Ferreira, L.G., 2002. Overview of the radiometric and biophysical performance of the MODIS vegetation indices. Remote Sens. Environ. 83 (1-2), 195–213.

Jankowski, K., Törnqvist, T., Fernandes, A., 2017. Vulnerability of Louisiana's coastal wetlands to present-day rates of relative sea-level rise. Nat. Commun. 8, 14792.

Jia, K., Jiang, W., Li, J., Tang, Z., 2018. Spectral matching based on discrete particle swarm optimization: A new method for terrestrial water body extraction using multi-temporal Landsat 8 images. Remote Sens. Environ. 209, 1–18.

Jia, M., Wang, Z., Mao, D., Ren, C., Wang, C., Wang, Y., 2021. Rapid, robust, and automated mapping of tidal flats in china using time series sentinel-2 images and google earth engine. Remote Sens. Environ. 255, 112285. https://doi.org/10.1016/j.rse.2021.112285.

Jiang, W.G., Yuan, L.H., Wang, W.J., Cao, R., Zhang, Y.F., Shen, W.M., 2015. Spatio-temporal analysis of vegetation variation in the Yellow River Basin. Ecol. Ind. 51, 117–126.

Kearney, M.S., Rogers, A.S., Townshend, J.R., Rizzo, E., Stutzer, D., Stevenson, J.C., Sundborg, K., 2002. Landsat imagery shows decline of coastal marshes in Chesapeake and Delaware Bays. Eos, Trans. Am. Geophys. Union 83 (16), 173–178.

Kirwan, M.L., Megonigal, J.P., 2013. Tidal wetland stability in the face of human impacts and sea-level rise. Nature 504 (7478), 53–60.

Kirwan, M.L., Temmerman, S., Skeehan, E.E., Guntenspergen, G.R., Fagherazzi, S., 2016. Overestimation of marsh vulnerability to sea level rise. Nat. Clim. Change 6 (3), 253–260.

Kopp, R.E., DeConto, R.M., Bader, D.A., Hay, C.C., Horton, R.M., Kulp, S., Oppenheimer, M., Pollard, D., Strauss, B.H., 2017. Evolving understanding of antarctic ice-sheet physics and ambiguity in probabilistic sea-level projections. Earth's Future 5 (12), 1217–1233.

Ladd, C.J.T., Duggan-Edwards, M.F., Bouma, T.J., Pagès, J.F., Skov, M.W., 2019. Sediment supply explains long-term and large-scale patterns in salt marsh lateral expansion and erosion. Geophys. Res. Lett. 46 (20), 11178–11187.

Langston, A.K., Vinent, O.D., Herbert, E.R., Kirwan, M.L., 2020. Modeling long-term salt marsh response to sea level rise in the sediment-deficient plum island estuary, ma. Limnol. Oceanogr. 9999, 1–16.

Lawrence, R. L., Wrlght, A. (2001). Rule-based classification systems using classification and regression tree (cart) analysis. Photogramm Eng Remote Sensing, 2001,67(10), 1137-1142.

Leonardi, N., Mei, X., Carnacina, I., Dai, Z., 2021. Marine sediment sustains the accretion of a mixed fluvial-tidal delta. Mar. Geol. 438, 106520. https://doi.org/10.1016/j.margeo.2021.106520.

Li, J. F., Feng, L. X., Xu, M., Yao, H. Y., Chen, W. (2011). The beach development and reclamation near the mouth bar channels in Changjiang Estuary. Proceedings of the 15th Chinese Oceanic Engineering Conference,1119-1124. (In Chinese with English abstract).

Li, H., Yang, S.L., 2009. Trapping effect of tidal marsh vegetation on suspended sediment, Yangtze Delta. J. Coastal Res. 25 (4), 915–924.

Li, X., Zhou, Y., Zhang, L., Kuang, R., 2014. Shoreline change of Chongming Dongtan and response to river sediment load: a remote sensing assessment. J. Hydrol. 511, 432–442.

Linhoss, A.C., Kiker, G., Shirley, M., Frank, K., 2015. Sea-level rise, inundation, and marsh migration: simulating impacts on developed lands and environmental systems. J. Coastal Res. 31 (1), 36–46.

Liu, J., Feng, Q., Gong, J., Zhou, J., Li, Y.i., 2016. Land-cover classification of the Yellow River Delta wetland based on multiple end-member spectral mixture analysis and a Random Forest classifier. Int. J. Remote Sens. 37 (8), 1845–1867.

Liu, Y.-F., Ma, J., Wang, X.-X., Zhong, Q.-Y., Zong, J.-M., Wu, W.-B., Wang, Q., Zhao, B., 2020. Joint effect of *Spartina alterniflora* invasion and reclamation on the spatial and temporal dynamics of tidal flats in Yangtze river estuary. Remote Sens. 12 (11), 1725. https://doi.org/10.3390/rs12111725.

Lovelock, C.E., Cahoon, D.R., Friess, D.A., Guntenspergen, G.R., Krauss, K.W., Reef, R., Rogers, K., Saunders, M.L., Sidik, F., Swales, A., Saintilan, N., Thuyen, L.X., Triet, T., 2015. The vulnerability of indo-pacific mangrove forests to sea-level rise. Nature 526 (7574), 559–563.

Lu, B., Jiang, X.Z., 2013. Reclamation impacts on the evolution of the tidal flat at Chongming Eastern Beach in Changjiang estuary. J. Remote Sens. 17 (2), 335–349.

Luo, X.X., Yang, S.L., Wang, R.S., Zhang, C.Y., Li, P., 2017. New evidence of Yangtze delta recession after closing of the Three Gorges Dam. Sci. Rep. 7, 41735.

Mei, X., Dai, Z., Wei, W., Li, W., Wang, J., Sheng, H., 2018. Secular bathymetric variations of the North Channel in the Changjiang (Yangtze) Estuary, China, 1880–2013: causes and effects. Geomorphology 303, 30–40.

Murray, N.J., Clemens, R.S., Phinn, S.R., Possingham, H.P., Fuller, R.A., 2014. Tracking the rapid loss of tidal wetlands in the Yellow Sea. Front. Ecol. Environ. 12 (5), 267–272.

Murray, N., Phinn, S., Clemens, R., Roelfsema, C., Fuller, R., 2012. Continental scale mapping of tidal flats across East Asia using the Landsat archive. Remote Sensing 4 (11), 3417–3426.

Murray, N.J., Phinn, S.R., DeWitt, M., Ferrari, R., Johnston, R., Lyons, M.B., Fuller, R.A., 2019. The global distribution and trajectory of tidal flats. Nature 565 (7738), 222–225.

Nardin, W., Edmonds, D.A., Fagherazzi, S., 2016. Influence of vegetation on spatial patterns of sediment deposition in deltaic islands during flood. Adv. Water Resour. 93, 236–248.

Okin, G.S., Gu, J., 2015. The impact of atmospheric conditions and instrument noise on atmospheric correction and spectral mixture analysis of multispectral imagery. Remote Sens. Environ. 164, 130–141.

Reed, D.J., 2002. Sea-level rise and coastal marsh sustainability: geological and ecological factors in the Mississippi delta plain. Geomorphology 48 (1-3), 233–243.

Rizzetto, F., Tosi, L., 2011. Aptitude of modern salt marshes to counteract relative sea-level rise, Venice lagoon (Italy). Geology 39 (8), 755–758.

Schuerch, M., Spencer, T., Temmerman, S., Kirwan, M.L., Wolff, C., Lincke, D., McOwen, C.J., Pickering, M.D., Reef, R., Vafeidis, A.T., Hinkel, J., Nicholls, R.J., Brown, S., 2018. Future response of global coastal wetlands to sea-level rise. Nature 561 (7722), 231–234.

Shaw, J.B., Mohrig, D., Wagner, R.W., 2016. Flow patterns and morphology of a prograding river delta. J. Geophys. Res. Earth Surf. 121 (2), 372–391.

Spencer, T., Schuerch, M., Nicholls, R.J., Hinkel, J., Lincke, D., Vafeidis, A.T., Reef, R., McFadden, L., Brown, S., 2016. Global coastal wetland change under sea-level rise and related stresses: the DIVA Wetland Change Model. Global Planet. Change 139, 15–30.

Tang, Z.H., Gu, Y., Dai, Z.J., Li, Y., LaGrange, T., Bishop, A., Drahota, J., 2015. Examining playa wetland inundation conditions for National Wetland Inventory, Soil Survey Geographic database, and LiDAR data. Wetlands 35 (4), 641–654.

Tian, B.o., Zhang, L., Wang, X., Zhou, Y., Zhang, W., 2010. Forecasting the effects of sea-level rise at chongming dongtan nature reserve in the yangtze delta, Shanghai, China. Ecol. Eng. 36 (10), 1383–1388.

Tucker, C.J., 1979. Red and photographic infrared linear combinations for monitoring vegetation. Remote Sens. Environ. 8 (2), 127–150.

van de Koppel, J., van der Wal, D., Bakker, J.P., Herman, P.M., 2004. Self-organization and vegetation collapse in salt marsh ecosystems. Am. Nat. 165 (1), E1–E12.

Vermote, E., Justice, C., Claverie, M., Franch, B., 2016. Preliminary analysis of the performance of the landsat 8/OLI land surface reflectance product. Remote Sens. Environ. 185, 46–56.

Vuik, V., Jonkman, S.N., Borsje, B.W., Suzuki, T., 2016. Nature-based flood protection: The efficiency of vegetated foreshores for reducing wave loads on coastal dikes. Coast. Eng. 116, 42–56.

Wang, H. M. (2010). Study on Risk Evaluation and Control Schemes of Land Subsidence in Shanghai City. Shanghai Geology, 031(004), 7-11,17. (In Chinese with English abstract).

Wei, W., Mei, X., Dai, Z., Tang, Z., 2016. Recent morphodynamic evolution of the largest uninhibited island in the Yangtze (Changjiang) estuary during 1998–2014: Influence of the anthropogenic interference. Cont. Shelf Res. 124, 83–94.

Wei, W., Dai, Z., Mei, X., Liu, J.P., Gao, S., Li, S., 2017. Shoal morphodynamics of the Changjiang (Yangtze) estuary: influences from river damming, estuarine hydraulic engineering and reclamation projects. Mar. Geol. 386, 32–43.

Wu, H., Zhu, J., 2010. Advection scheme with 3rd high-order spatial interpolation at the middle temporal level and its application to saltwater intrusion in the Changjiang Estuary. Ocean Model 33 (1-2), 33–51.

Xiao, X., Hollinger, D., Aber, J., Goltz, M., Davidson, E.A., Zhang, Q., Moore, B., 2004. Satellite-based modeling of gross primary production in an evergreen needleleaf forest. Remote Sens. Environ. 89 (4), 519–534.

Xu, H., 2006. Modification of normalized difference water index (NDWI) to enhance open water features in remotely sensed imagery. Int. J. Remote Sens. 27 (14), 3025–3033.

Yan, H., Dai, Z., Li, J., Zhao, J., Zhang, X., Zhao, J., 2011. Distributions of sediments of the tidal flats in response to dynamic actions, Yangtze (Changjiang) Estuary. J. Geog. Sci. 21 (4), 719–732.

Yang, S.L., Luo, X., Temmerman, S., Kirwan, M., Bouma, T., Xu, K., Zhang, S., Fan, J., Shi, B., Yang, H., Wang, Y.P., Shi, X., Gao, S., 2020. Role of delta-front erosion in sustaining salt marshes under sea-level rise and fluvial sediment decline. Limnol. Oceanogr. 65 (9), 1990–2009.

Yang, H.F., Yang, S.L., Li, B.C., Wang, Y.P., Wang, J.Z., Zhang, Z.L., Xu, K.H., Huang, Y. G., Shi, B.W., Zhang, W.X., 2021. Different fates of the yangtze and mississippi deltaic wetlands under similar riverine sediment decline and sea-level rise. Geomorphology 381, 107646. https://doi.org/10.1016/j.geomorph.2021.107646.

Yang, S.L., Zhao, Q.Y., Ding, P.X., Zhu, J., 2002. Annual changes in coastal dynamic and SSC processes as well as their statistic relationships to intertidal bed-level: Shanghai Coast. Mar. Sci. 26 (2), 37–41. In Chinese with English Abstract.

Yuan, L., Zhang, L., Xiao, D., Huang, H., 2011. The application of cutting plus waterlogging to control Spartina alterniflora on saltmarshes in the Yangtze Estuary, China. Estuar. Coast. Shelf Sci. 92 (1), 103–110.

Yun, C.X., 2004. Regulations of recent evolution of Yangtze Estuary. Ocean Press 11–14. In Chinese.

Zhang, X.i., Xiao, X., Wang, X., Xu, X., Chen, B., Wang, J., Ma, J., Zhao, B., Li, B.o., 2020. Quantifying expansion and removal of spartina alterniflora on Chongming island, china, using time series Landsat images during 1995–2018. Remote Sens. Environ. 247, 111916. https://doi.org/10.1016/j.rse.2020.111916.

Zhu, Z., Woodcock, C.E., 2012. Object-based cloud and cloud shadow detection in Landsat imagery. Remote Sens. Environ. 118, 83–94.

Zhu, Z., Zhang, L., Wang, N., Schwarz, C., Ysebaert, T., 2012. Interactions between the range expansion of saltmarsh vegetation and hydrodynamic regimes in the Yangtze Estuary, China. Estuar. Coast. Shelf Sci. 96, 273–279.